Available online at ScienceDirect

Nuclear Engineering and Technology

journal homepage: www.elsevier.com/locate/net

Original Article

Influence of Dynamic Strain Aging on Tensile Deformation Behavior of Alloy 617

I.M.W. Ekaputra [a,*], Woo-Gon Kim [b], Jae-Young Park [b], Seon-Jin Kim [a], and Eung-Seon Kim [b]

[a] Pukyong National University, 365, Shinsuro, Nam-gu, Busan 608-739, South Korea
[b] Korea Atomic Energy Research Institute, 989-111 Daedokdaero, Yuseong-gu, Daejeon, 305-353, South Korea

ARTICLE INFO

Article history:
Received 18 March 2016
Received in revised form
14 June 2016
Accepted 20 June 2016
Available online 12 July 2016

Keywords:
Alloy 617
Dynamic Strain Aging
Ludwigson
Serration
Tensile Curves

ABSTRACT

To investigate the dynamic strain aging (DSA) behavior of Alloy 617, high-temperature tensile tests were carried out with strain rates variations of 10^{-3}/s, 10^{-4}/s, and 10^{-5}/s from 24°C to 950°C. Five flow relationships, Hollomon, Ludwik, Swift, Ludwigson, and Voce, were applied to describe the tensile true stress–strain curves, and the DSA region was defined. In describing the tensile curves, Ludwigson's equation was superior to the other equations, and the DSA region was adequately defined by this equation as plateaus at intermediate temperatures from 200°C to 700°C. It was identified that Alloy 617 is dominated by three types of serrations, known as Types D, A+B, and C. The activation energy values for each serration type were obtained by the Arrhenius equation. By using the obtained activation energy values, the serrated yielding map and the DSA mechanism were drawn and manifested. In addition, the relationship between the tensile strength and strain rate at higher temperatures above 700°C was found to be closely related to the amounts of slip lines. In the scanning electron microscope (SEM) fractographs, there was a significant difference at the low, intermediate, and high temperatures, but almost the same to the three strain rates.

1. Introduction

A very high temperature reactor (VHTR) is currently being researched as one of the promising candidates for Generation IV (Gen IV) reactors to economically produce electricity and hydrogen [1]. A lot of aspects should be considered for developing this VHTR system because the goals are to achieve a highly economical, proliferation-resistant reactor with enhanced safety and minimal waste. The VHTR system consists of several major components such as a control rod system (CRS), a reactor pressure vessel (RPV), a hot gas duct (HGD), and an intermediate heat exchanger (IHX), as shown in Fig. 1. The IHX is designed with a life span of 60 years under operating conditions up to 950°C [1–5]. It is very crucial to choose an appropriate material which has superior

* Corresponding author.
E-mail address: wgkim@kaeri.re.kr (I.M.W. Ekaputra).
http://dx.doi.org/10.1016/j.net.2016.06.013

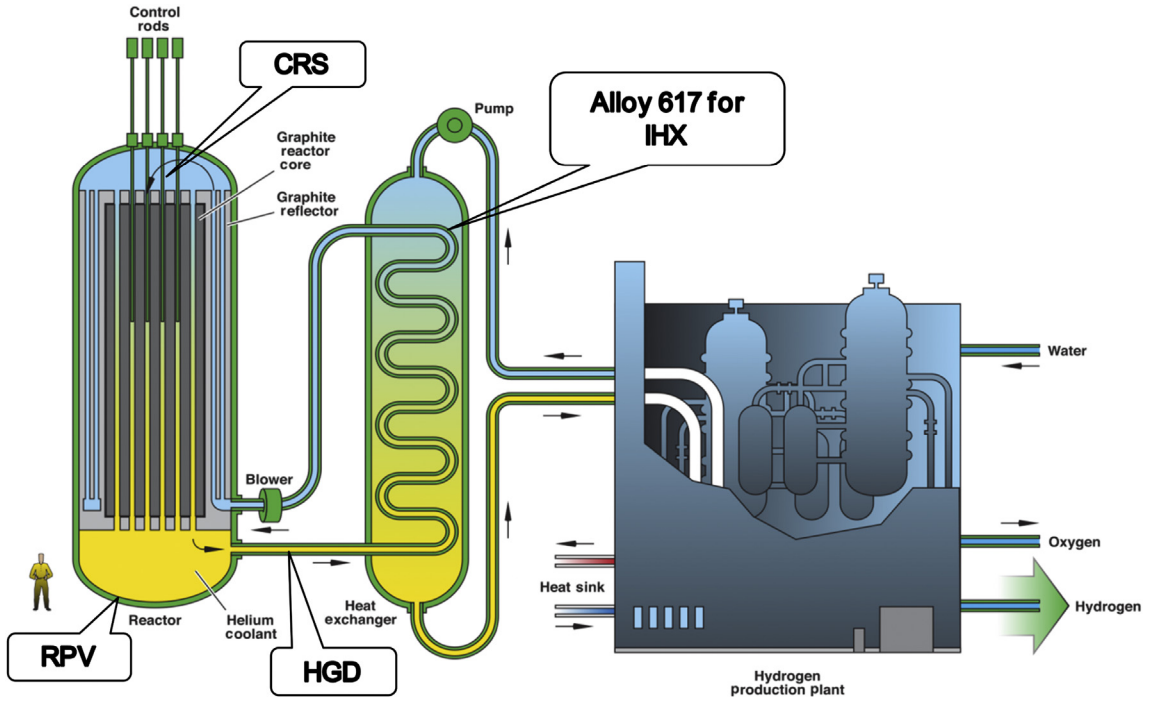

Fig. 1 – Schematic illustration of very high temperature reactor (VHTR). CRS, control rod system; HGD, hot gas duct; IHX, intermediate heat exchanger; RPV, reactor pressure vessel.

mechanical properties against severe temperature conditions for a long service time.

Nickel-based super-alloys have been proposed for use in VHTR components. Among these alloys, Alloy 617 is considered as one of the prime candidates for the IHX, due to its advanced mechanical properties [1–5]. Investigation into these mechanical properties should be carried out comprehensively for design and safety considerations, because a significant degradation of mechanical properties may occur due to a serrated yielding phenomenon in high-temperature environments [6,7]. This phenomenon results in strain localization that can affect crack initiation and propagation under upset conditions with sudden increases in applied mechanical stresses [8]. The serrated yielding is caused by a dynamic strain aging (DSA) or Portevin–Le Chatelier (PLC) effect, and is found in a uniaxial tensile load at particular temperatures and strain-rate conditions. The DSA effect is indicated by a nonuniform deformation which is controlled by diffusion. It results from the interaction between solute atoms and mobile dislocation, whereas the mobile dislocation is temporarily arrested by solute atoms in the slip path [9–11].

In this study, the DSA behavior of Alloy 617 under tensile stress–strain was investigated. A series of tensile data was obtained from the tensile tests at temperatures ranging from 24°C to 950°C with the three strain rates of 10^{-3}/s, 10^{-4}/s, and 10^{-5}/s. Five flow relationships, Hollomon, Ludwik, Swift, Ludwigson, and Voce, were applied to describe the tensile true stress–strain curves. The DSA region of Alloy 617 was defined, and its mechanism was discussed from the activation energy values, which were obtained by applying the Arrhenius equation. In addition, fracture microstructures were observed by optical microscope (OM) and scanning electron microscope (SEM).

2. Materials and methods

The raw material of commercial grade Alloy 617 (Haynes 617, hereafter Alloy 617) was a hot-rolled plate with a thickness of 15.875 mm (5/8 inch). Its chemical composition is listed in Table 1. The tensile-test specimens were fabricated in a cylindrical form with a 30-mm-gauge length and 6-mm diameter with stress axis in the rolling direction. All specimens were polished along a specimen axis by employing #1000-grit sand paper.

The tension tests were performed using a universal testing machine with a 100-kN capacity (model: RB Unitech-M, R&B Inc., Daejeon, Republic of Korea), and a screw-driven load frame at constant crosshead velocities corresponding to strain rates of 10^{-3}/s, 10^{-4}/s, and 10^{-5}/s. It must be noted that because the strain rates were determined from the original gauge length, the strain rates might have dropped as the specimen was extended during the testing. The tension loading of stresses was applied to a specimen using an AC servomotor type. The main components of apparatus were composed of a three-zone heating furnace, temperature controller, data acquisition system (PC and monitor), and program controller. The test temperatures were controlled within ± 2°C and a thermocouple was attached to the gauge section of specimen. Microstructures of the fractured

Table 1 – Chemical compositions of Alloy 617 (wt. %).

C	Ni	Fe	Si	Mn	Co	Cr
0.08	53.11	0.949	0.084	0.029	12.3	22.2
Ti	P	S	Mo	Al	B	Cu
0.41	0.003	0.002	9.5	1.06	< 0.002	0.0268

specimens were observed using an optical microscope (OM, OLYMPUS GK-51, Japan) and a scanning electron microscope (SEM, JEOL JSM-6300, Japan).

3. Results and discussion

3.1. The DSA region

Fig. 2 shows a typical plot of experimental engineering stress–strain curves obtained at wide temperature ranges from 24°C to 950°C with strain rate of 10^{-4}/s. It is shown that the ultimate tensile strength (σ_{UTS}) values decrease with an increase in temperature. The strain values from σ_{UTS} to fracture tend to increase with an increase in temperature. The tensile stress–strain curves from 200°C to 700°C are observed to fall narrowly. It is also observed that three different types of serrations appear at these temperature regions. Three serrations types for Alloy 617 are identified as Types D, A+B, and C, as specifically shown in Fig. 3. Type D initially appears at 200°C, and followed by Type A+B from 300°C to 500°C. Type A+B is defined as the combination of Types A and B, where Type A appears initially and then it is followed by Type B at the higher strain value. Type C appears in the range from 600°C to 700°C, and beyond these temperatures, no serrations are observed. According to Rodriguez [6], five serrations types have been adequately described as Types A, B, C, D, and E. Type A is acknowledged by a sudden increase in stress at the onset of serrated yielding, followed by a sequence of rapid decrease below the average of the tensile stress–strain curve. The serrated yielding continues periodically in the plastic region of the tensile stress–strain curve. For Type B, the serrated yielding process is almost the same with Type A. However, the serrated yielding oscillates about the average level of the tensile stress–strain curve continuously in quick succession. It was reported that the quick succession occurred due to the high diffusivity rate of solute atoms in Type B [6,7,9]. Type C is identified as a sudden decrease in stress at onset of serrated yielding, followed by a rapid increase to the average level of the tensile stress–strain curve. Type D is characterized by the occurrence of plateaus in the tensile stress–strain curve. For Type E, the serrated yielding is normally found after Type A at a higher strain [6]. Serrations types for Alloy 617 are mainly dominated by three types of serrations as Types D, A+B, and C.

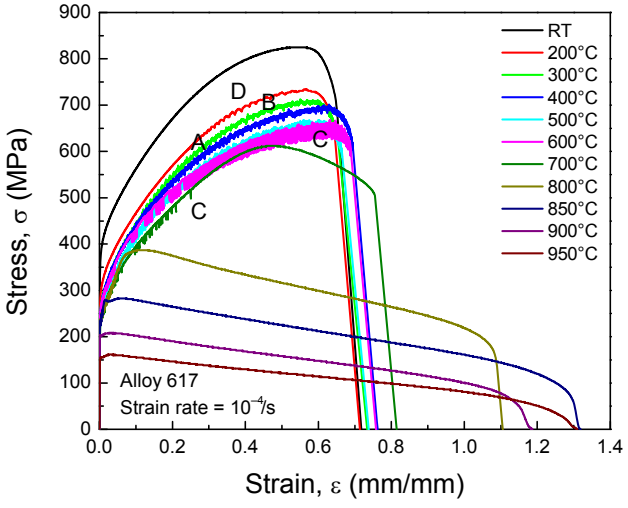

Fig. 2 – Engineering stress–strain for different temperatures at 10^{-4}/s. RT, room temperature.

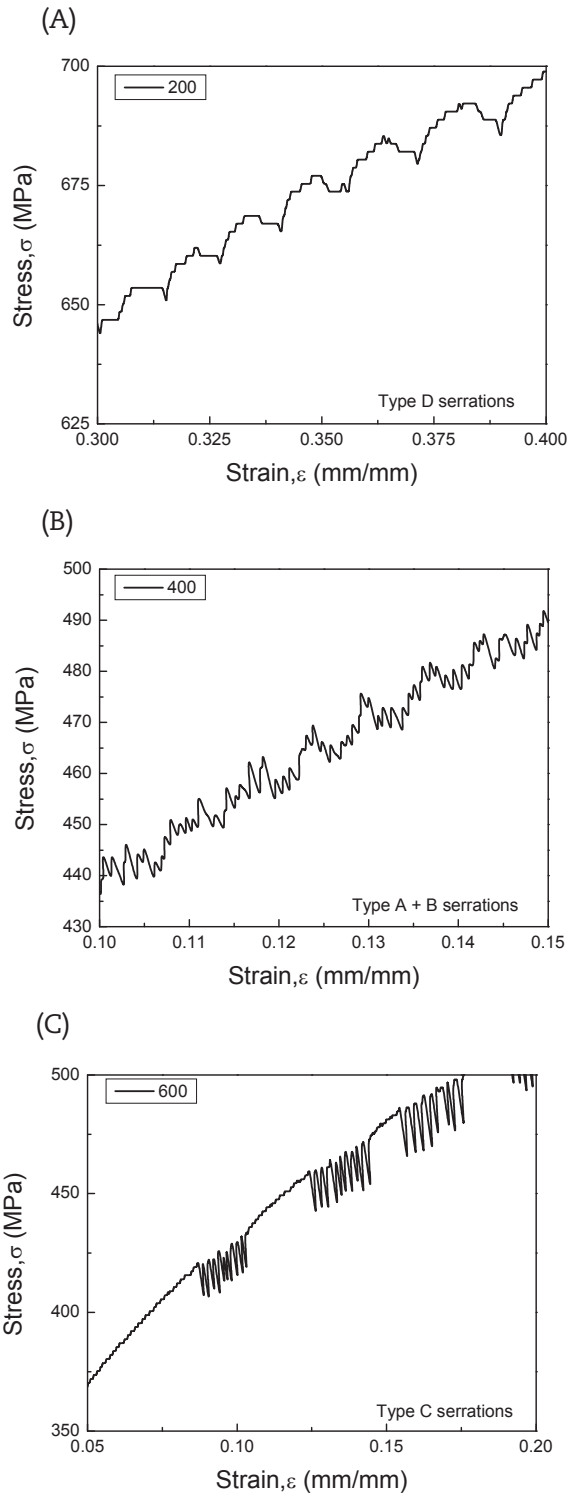

Fig. 3 – Three types of serrations at DSA region. (A) Type D. (B) Type A+B. (C) Type C. DSA, dynamic strain aging.

Fig. 4 shows double logarithmic plots of the true stress as a function of the true strain for 10^{-4}/s strain rate at different

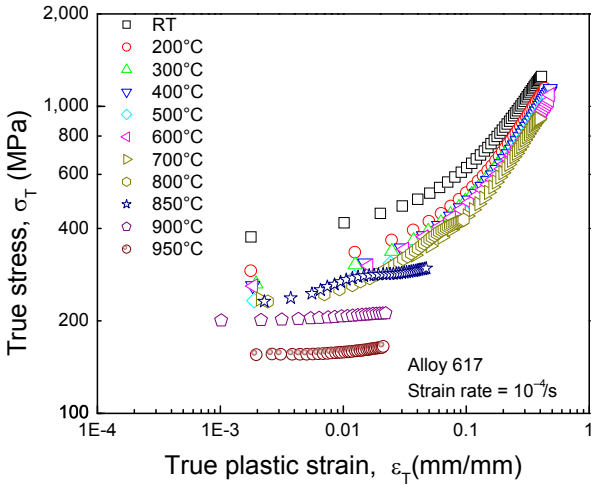

Fig. 4 – True stress–plastic strain for different temperatures at 10^{-4}/s. RT, room temperature.

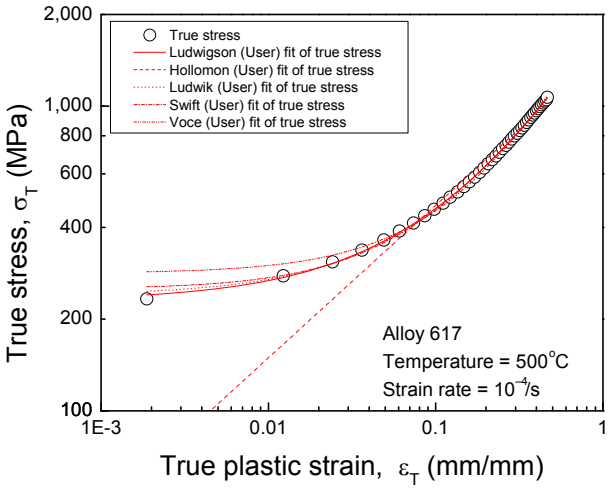

Fig. 6 – Curve fit lines by flow relationships for 10^{-4}/s at 500°C.

temperatures. At the first temperature region, the true stress values decrease with an increase in temperature from 24°C to 200°C. A marginal decrease is observed narrowly at the second temperature region from 200°C to 700°C. With further increases in temperature in the third temperature region from 700°C to 950°C, a rapid decrease is observed in true stress values. According to these, three temperature regions for Alloy 617 are categorized as the low, intermediate, and high temperatures. A similar trend was also observed for the different strain-rate conditions.

The DSA region is described specifically by applying the five flow relationships: Hollomon, Ludwik, Swift, Ludwigson, and Voce [12–14]. These flow relationships are given in the following Eqs. (1) to (5). For Hollomon, it is expressed as:

$$\sigma = K_H \varepsilon^{n_H}, \tag{1}$$

where σ is the stress (MPa), ε is the plastic strain (mm/mm), n_H is the strain-hardening exponent, and K_H is the strain-hardening coefficient. For Ludwik, it is expressed as:

$$\sigma = \sigma_0 + K_L \varepsilon^{n_L}, \tag{2}$$

where n_L is the strain-hardening exponent, K_L is the strain-hardening coefficient, and σ_0 is a constant stress (MPa). For Swift, it is expressed as:

$$\sigma = K_S(\varepsilon_0 + \varepsilon)^{n_S}, \tag{3}$$

where n_S is the strain-hardening exponent, K_S is the strain-hardening coefficient, and ε_0 is a constant strain (mm/mm). For Ludwigson, it is expressed as:

$$\sigma = K_1 \varepsilon^{n_1} + \exp(K_2 + n_2 \varepsilon), \tag{4}$$

where K_1 and K_2 are the strain-hardening coefficients, and n_1 and n_2 are the strain-hardening exponents. Then, for Voce, it is expressed as:

$$\sigma = \sigma_S - (\sigma_S - \sigma_1)\exp(n_V \varepsilon), \tag{5}$$

where σ_S is the saturation stress (MPa), σ_1 is the stress at the

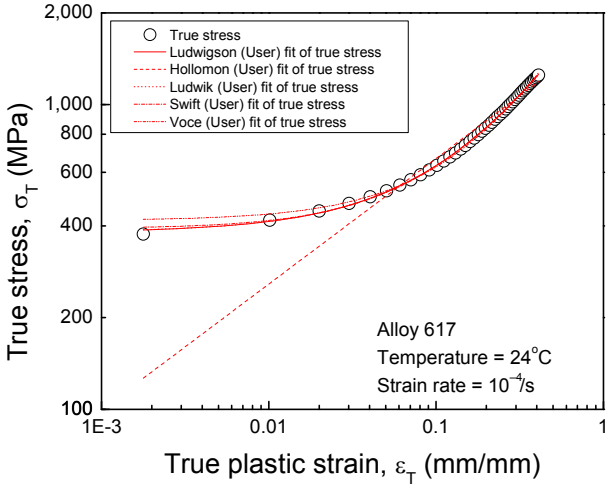

Fig. 5 – Curve fit lines by flow relationships for 10^{-4}/s at 24°C.

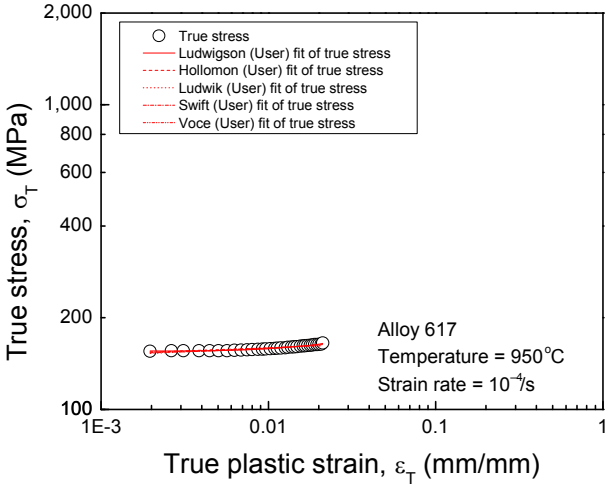

Fig. 7 – Curve fit lines by flow relationships for 10^{-4}/s at 950°C.

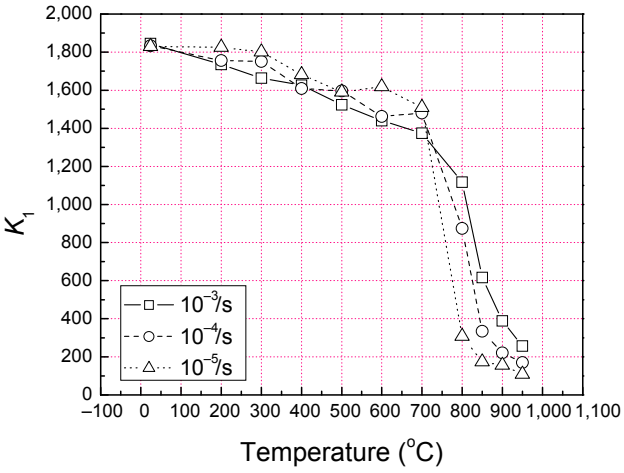

Fig. 8 – Variation of strain-hardening coefficient K_1 with temperature for different strain rates.

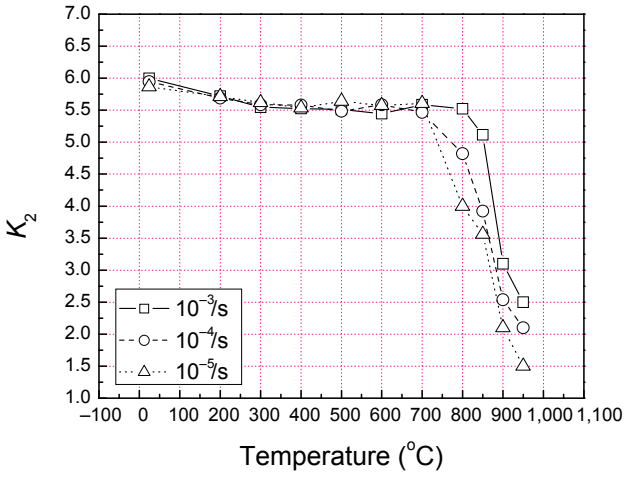

Fig. 10 – Variation of strain-hardening coefficient K_2 with temperature for different strain rates.

onset of plastic deformation (MPa), and n_V is the strain-hardening exponent.

The applicability of these flow relationships depends on the steel types and test conditions. For example, Voce's equation adequately described the tensile true stress–strain for 9Cr–1Mo stainless steel (SS) under a wide range of temperatures and strain rates [13,14]. For type 316(N) SS, Ludwigson's equation was proper for describing the tensile true stress–strain at low temperatures [12], whereas both Ludwigson and Voce were able to describe the tensile true stress–strain very well at intermediate and high temperatures [12].

Figs. 5–7 show the typical curve fits of five different flow relationships at three representative temperature regions with a strain rate of 10^{-4}/s. It can be seen that the behavior of experimental data is different at low, intermediate, and high temperatures. The curvilinear curves are shown at room and intermediate temperatures, whereas the curves are nearly straight lines at high temperatures. By considering the R^2 (coefficient of determination) values, the goodness-of-fit lines are evaluated using five flow relationships. From the results, it is found that, of the five equations, Ludwigson's equation is the best to describe the tensile true stress–strain curves. It is known that an R^2 value close to 1 has a small residual or deviation to the experimental data, whereas an R^2 value close to 0 has a big residual. Following Ludwigson's equation, the DSA region of Alloy 617 is observed by its coefficients and exponents as plateaus at intermediate temperatures from 200°C to 700°C. Figs. 8–11 show the variations of K_1, K_2, n_1, and n_2 with temperature at the three strain rates of 10^{-3}/s, 10^{-4}/s, and 10^{-5}/s. It is shown that a strain rate dependence on temperature is observed at intermediate and high temperatures. At intermediate temperatures, a systematic increase in K_1, K_2, n_1, and a systematic decrease in n_2 are shown with a decrease in strain rate. At high temperatures, a systematic decrease in K_1, K_2, and n_1 is shown with a decrease in strain rate. Otherwise, the n_2 increases with a decrease in strain rate at high temperatures. It was reported that a rapid increase in n_2 could be caused by a change in controlling mechanism from cross-slip to dislocation climb at high temperatures [14].

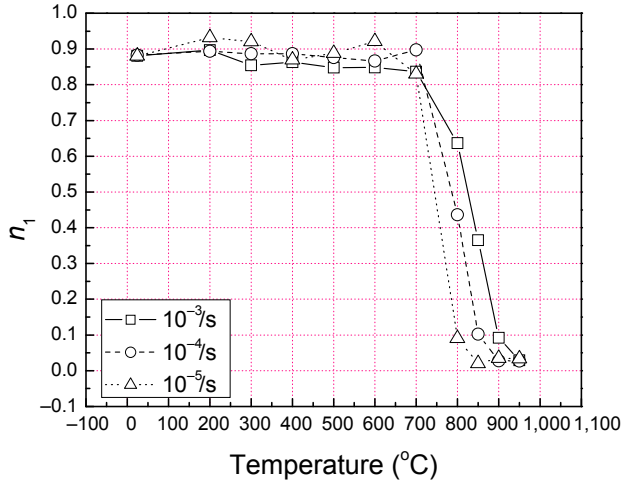

Fig. 9 – Variation of strain-hardening exponent n_1 with temperature for different strain rates.

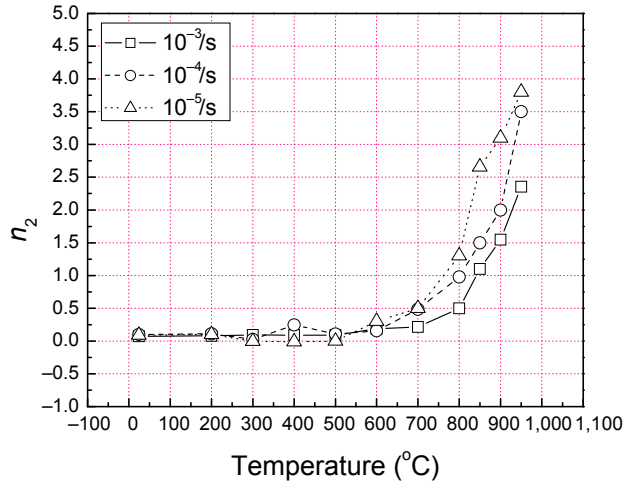

Fig. 11 – Variation of strain-hardening exponent n_2 with temperature for different strain rates.

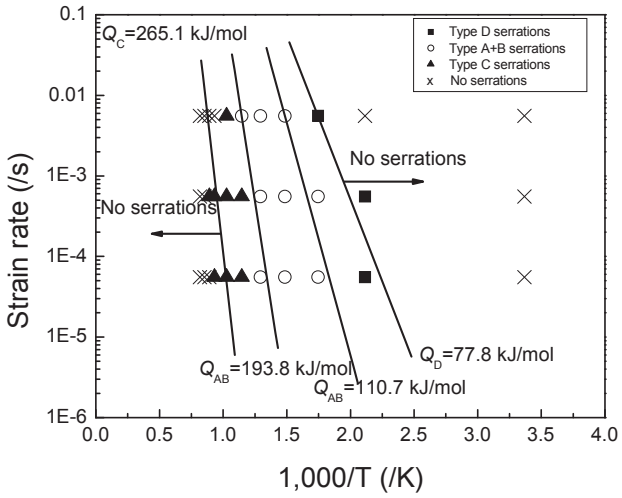

Fig. 12 – Serrated yielding map under tensile loading.

3.2. *The DSA mechanism*

Generally, the DSA mechanism can be evaluated from the activation energy values and comparing them with those values reported in the literature, because the DSA is the thermally activated process associated with interaction between diffusing solute atoms and mobile dislocation [15–19]. Five methods are usually used to calculate the activation energy. These five methods consist of (1) the Arrhenius equation from the dependence of temperatures and strain rates to the onset of serrated yielding, (2) the temperature and strain rate dependence to the critical plastic strain method, (3) the stress drop method ($\Delta\sigma$), (4) McCormick's strain aging model, and (5) the intercept method. By using these five methods, the average activation energy can be evaluated to determine the DSA mechanism. It was reported that the evaluation of activation energy values, using the different methods, was in good agreement with each other [15]. As there is no significant difference, the author applies only one method for the practical evaluation.

Fig. 12 shows the derivation of activation energy obtained by the Arrhenius equation from the dependence of temperatures and strain rates to the onset of serrated yielding. The

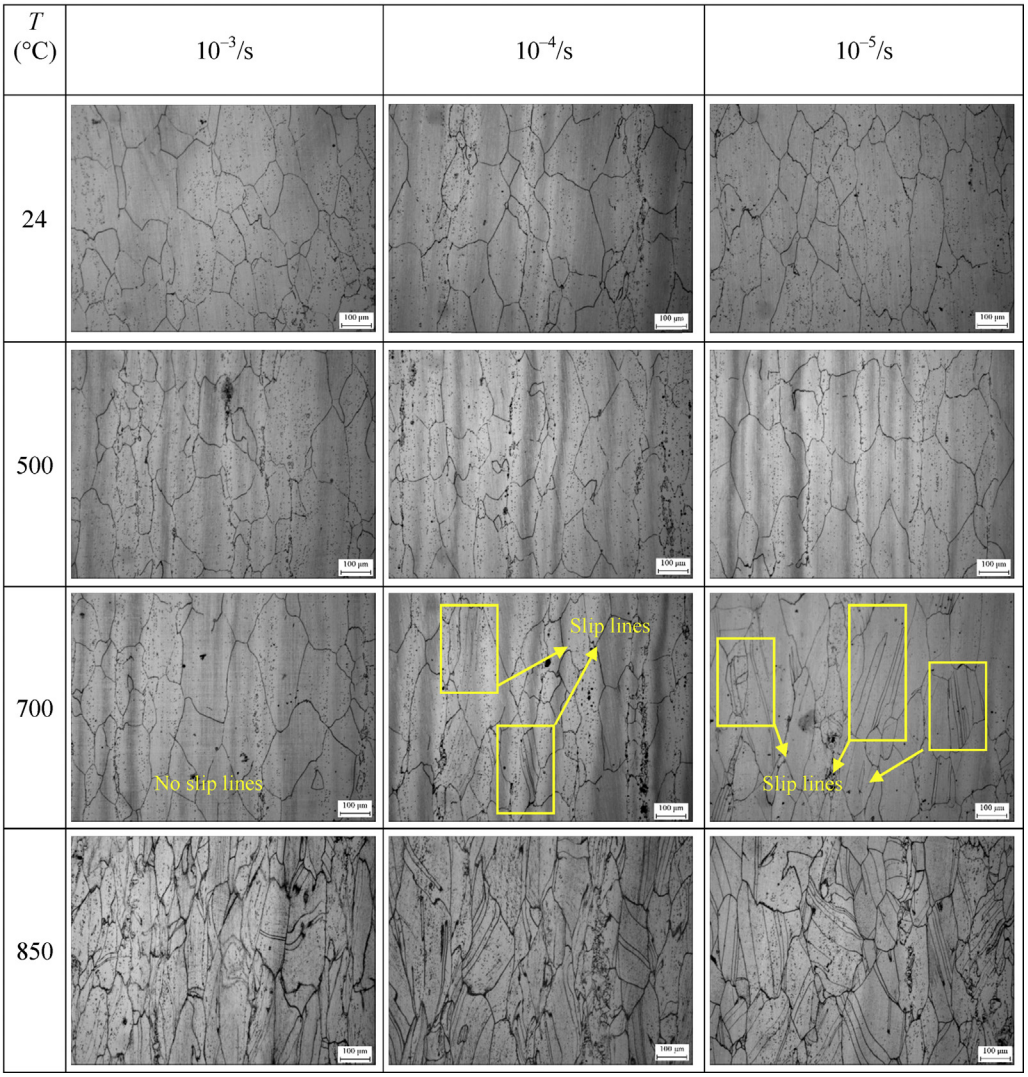

Fig. 13 – OM photos of Alloy 617 at the wide range temperatures and strain rates. OM, optical microscope.

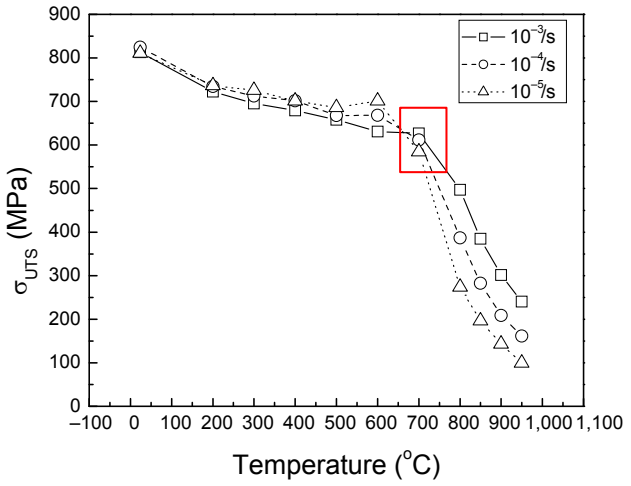

Fig. 14 – Variation of ultimate tensile strength with temperature for different strain rates.

regression lines are fitted for the onset of each serration type by applying the Arrhenius equation as [12],

$$\frac{d\varepsilon}{dt} = A \exp\left(\frac{Q}{RT}\right), \quad (6)$$

where R is the gas constant (8.314 J/mol/K), T is the temperature (K), Q is the apparent activation energy (kJ/mol), and A is a constant. The activation energy for the onset of serrated yielding is obtained from the slope of regression line (Q = slope × R), as shown in Fig. 12.

According to the activation energy values, the DSA mechanism for Alloy 617 will be mostly caused by the lattice and pipe diffusion of solute atoms. It is a good agreement with the result from other studies that the DSA mechanisms in Ni and Ni-based alloys have mostly been attributed to lattice and pipe diffusion [16,20–22]. For Type D serrations, the activation energy is 77.8 kJ/mol, where the pipe diffusion of interstitial solute atoms, such as carbon, through the dislocation core is responsible for the DSA mechanism. For the combination of Type A+B serrations, the activation energy ranges from 110.7 kJ/mol to 193.8 kJ/mol, where the lattice diffusion of interstitial solute atoms, such as carbon, is responsible. For Type C serrations, the activation energy is 265.1 kJ/mol, where the lattice diffusion of substitutional solute atoms, such as chromium, is responsible.

3.3. *Microstructures*

Fig. 13 shows typical OM photos observed for tensile elongated microstructures at different temperatures and strain rates. In the OM photos at 24°C and 500°C, slip lines are not observed, but at 700°C, some slip lines are observed at 10^{-5}/s and 10^{-4}/s, but no slip line is observed at 10^{-3}/s. Also, at 850°C, many slip lines are observed regardless of the three strain rates, and particularly their amounts are higher at 10^{-5}/s than those of 10^{-3}/s, and 10^{-4}/s. It has been reported that additional deformation mechanisms in Alloy 617, such as creep and dynamic recrystallization, occurred during tensile deformation at the higher temperatures [23,24]. Eventually, these mechanisms will result in the creation of slip lines after the completion of

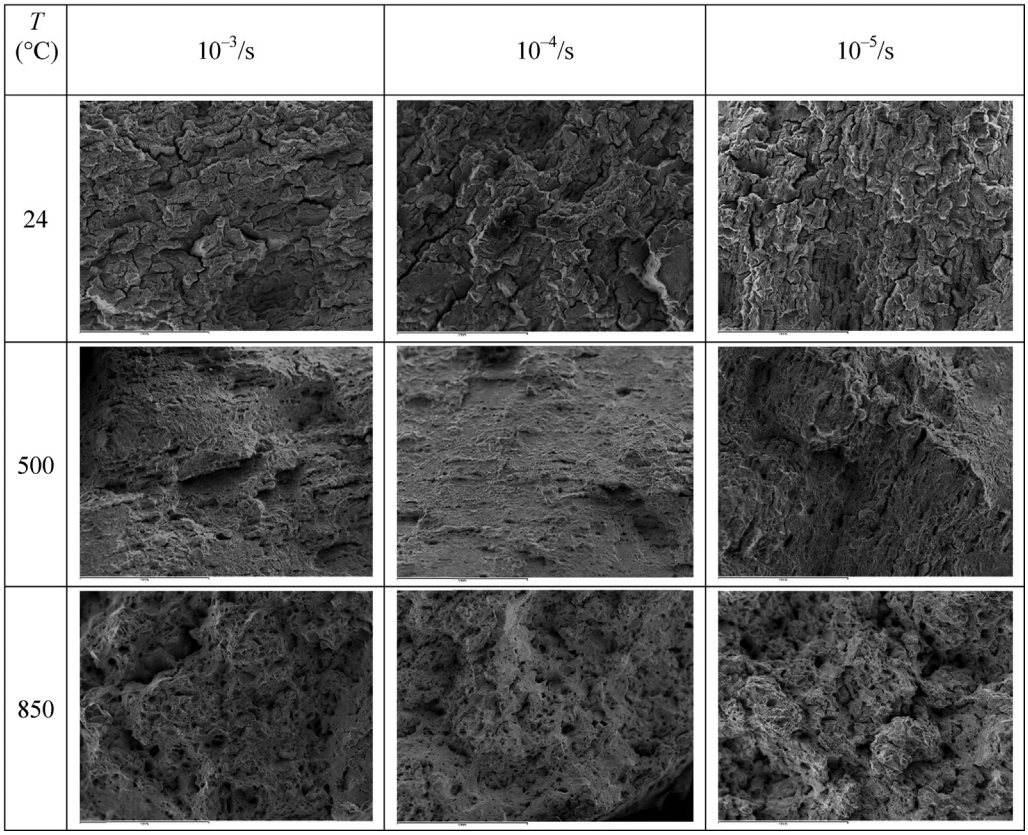

Fig. 15 – Fracture surfaces of Alloy 617 in a wide range of temperatures and strain rates with 50× magnification.

the test as shown in Fig. 13, and they are responsible for a significant decrease in material strength and an increase in ductility. As shown in Fig. 14, the relationship between the tensile strength and strain rate at the higher temperatures above 700°C is found to be closely related to amounts of slip lines. Namely, the σ_{UTS} values show a rapid decrease from 800°C to 950°C for all strain rates, and decrease with decreases in strain rates. Moreover, it is observed that the ductility values increase with increasing temperature, as shown in Fig. 2. Temperatures up to 700°C show a little ductility or necking, indicated by the small strain value beyond the σ_{UTS}, whereas significant ductility is shown in the range of temperatures from 800°C to 950°C. Fig. 15 shows typical SEM microstructures observed at different temperatures and strain rates. It appears that there is a significant difference at the low, intermediate, and high temperatures, but almost the same to the three strain rates. At the low and intermediate temperatures of 24°C and 500°C, the fracture surface seems almost flat, similar to a cleavage fracture. However, at the high temperature of 850°C, many voids occur in the fracture surface as a ductile fracture.

4. Conclusion

To investigate the dynamic strain aging (DSA) behavior of Alloy 617, the tensile tests were carried out with the variations of strain rates of 10^{-3}/s, 10^{-4}/s, and 10^{-5}/s at a wide temperature range of 24°C to 950°C. Five flow relationships, Hollomon, Ludwik, Swift, Ludwigson, and Voce, were applied to describe the tensile true stress–strain curves and the DSA behavior was investigated. From the results, the following conclusions may be drawn: (1) In describing the tensile stress–strain curves, Ludwigson's equation was superior to the other equations, and three temperature regions were identified as low (24–200°C), intermediate (200–700°C), and high temperatures (700–950°C). The DSA region was adequately defined by Ludwigson's equation as marginal increases or decreases appeared like plateaus at intermediate temperatures from 200°C to 700°C. (2) From the tensile stress–strain curves, it was identified that Alloy 617 was dominated by three types of serrations; Types D, A+B, and C. Type D serrations appeared at lower temperatures, followed by Type A+B, and Type C at higher temperatures. (3) The activation energy values for each serration type were obtained on the basis of the Arrhenius equation from the dependence of temperature and strain rate on the onset of serrated yielding. The serrated yielding map and the DSA mechanism were drawn and manifested well. (4) The relationship between tensile strength (σ_{UTS}) and strain rates exhibited a good correlation at higher temperatures above 700°C. The reason for this was that many slip lines occurred at the low strain rates of higher temperatures above 700°C.

Conflicts of interest

All authors have no conflicts of interest to declare.

Acknowledgments

This study was supported by Nuclear Research & Development Program of the National Research Foundation of Korea (NRF), grant funded by the Korean government (MSIP) (grant code: NRF-2012M2A8A2 025682).

REFERENCES

[1] W.G. Kim, J.Y. Park, I.M.W. Ekaputra, S.J. Kim, M.H. Kim, Y.W. Kim, Creep deformation and rupture behavior of Alloy 617, Eng. Fail. Anal. 58 (2015) 441–451.
[2] W.G. Kim, J.Y. Park, I.M.W. Ekaputra, S.D. Hong, S.J. Kim, Y.W. Kim, Comparative study on the high-temperature tensile and creep properties of Alloy 617 base and weld metals, J. Mech. Sci. Technol. 27 (2013) 2331–2340.
[3] W.G. Kim, J.Y. Park, I.M.W. Ekaputra, M.H. Kim, Y.W. Kim, Analysis of creep behavior of Alloy 617 for use of VHTR system, Proc. Mater. Sci. 3 (2014) 1285–1290.
[4] W.G. Kim, S.N. Yin, J.Y. Park, S.D. Hong, Y.W. Kim, An improved methodology for determining tensile design strengths of Alloy 617, J. Mech. Sci. Technol. 26 (2012) 379–387.
[5] W.G. Kim, J.Y. Park, S.J. Kim, M.H. Kim, Improved methodology for determining tensile elastic and plastic strain components of Alloy 617, J. Mech. Sci. Technol. 28 (2014) 3027–3032.
[6] P. Rodriguez, Serrated plastic flow, Bull. Mater. Sci. 6 (1984) 653–663.
[7] R.A. Mulford, U.F. Kocks, New observations on the mechanics of dynamic strain aging and of jerky flow, Acta Metall. 27 (1979) 1125–1134.
[8] M. Ivanchenko, Y. Yagodzinskyy, U. Ehrnstèn, W. Karlsen, H. Hänninen, Manifestations of DSA in austenitic stainless steels and Inconel alloys, in: 20th International Conference on Structural Mechanics in Reactor Technology (SMiRT 20), 2009, pp. 1–9.
[9] G.G. Saha, P.G. McCormick, P. Rama Rao, Portevin-Le Chatelier effect in an Al–Mn Alloy I: serration characteristics, Mater. Sci. Eng. 62 (1984) 187–196.
[10] A. Van Den Beukel, Theory of the effect of dynamic strain aging on mechanical properties, Phys. Stat. So. 30 (1975) 197–206.
[11] K.G. Samuel, S.L. Mannan, P. Rodriguez, Serrated yielding in AISI 316 stainless steel, Acta Metall. 36 (1988) 2323–2327.
[12] E. Issac Samuel, B.K. Choudhary, K. Bhanu Sankara Rao, Influence of temperature and strain rate on tensile work hardening behavior of Type 316LN austenitic stainless steel, Scr. Mater. 46 (2002) 507–512.
[13] D.P. Rao Palaparti, B.K. Choudhary, E. Issac Samuel, V.S. Srinivasan, M.D. Mathew, Influence of strain rate and temperature on tensile stress–strain and work hardening behavior of 9Cr–1Mo ferritic steel, Mater. Sci. Eng. A 538 (2012) 110–117.
[14] B.K. Choudhary, D.P. Rao Palaparti, E. Isaac Samuel, Analysis for the tensile stress–strain and work-hardening behavior in 9Cr–1Mo steel, Metall. Mater. Trans A 44 (2013) 212–223.
[15] S.G. Hong, S.B. Lee, Mechanism of dynamic strain aging and characterization of its effect on the low-cycle fatigue behavior in Type 316LN stainless steel, J. Nucl. Mater. 340 (2005) 307–314.
[16] C.L. Hale, W.S. Rolling, M.L. Weaver, Activation energy calculations for discontinuous yielding in Inconel 718SPF, Mater. Sci. Eng. A 300 (2001) 153–164.

[17] S. Venkadesan, C. Phantraj, P.V. Sivaprasad, P. Rodriguez, Activation energy for serrated flow in a 15Cr–15Ni modified austenitic stainless steel, Acta Metall. Mater. 40 (1992) 569–580.
[18] W. Chen, M.C. Chaturvedi, On mechanism of serrated deformation in aged Inconel 718, Mater. Sci. Eng. A 229 (1997) 163–168.
[19] Reza Sharghi-Moshtaghin, Sirous Asgari, The characteristics of serrated flow in superalloy IN738LC, Mater. Sci. Eng. A 486 (2008) 376–380.
[20] E.A. Brandes, G.B. Brook, Smithells Metal Reference Book, seventh ed., Butterworth-Heinemann, Oxford, 1992.
[21] J. Čermăk, H. Mehrer, Tracer diffusion of 14C in austenitic Ni–Fe–Cr Alloys, Acta Metall. Mater. 42 (1994) 1345–1350.
[22] D.D. Pruthi, M.S. Anand, R.P. Agarwala, Diffusion of chromium in Inconel-600, J. Nucl. Mater. 64 (1977) 206–210.
[23] Udo Bruch, Dieter Schuhmacher, Philip J. Ennis, Eberhard te Heesen, Tensile and impact properties of candidate alloys for high-temperature gas-cooled reactor applications, Nucl. Technol. 66 (1984) 357–362.
[24] D. Kaoumi, K. Hrutkay, Tensile deformation behavior and microstructure evolution of Ni-based superalloy 617, J. Nucl. Mater. 454 (2014) 265–273.